JOURNAL OF GUIDANCE, CONTROL, AND DYNAMICS
Vol. 19, No. 3, May–June 1996

Attitude Determination and Control of Clementine During Lunar Mapping

Glenn Creamer*
Swales and Associates, Inc., Beltsville, Maryland 20705
and
Paul DeLaHunt,† Steve Gates,‡ and Marv Levenson§
U.S. Naval Research Laboratory, Washington, D.C. 20375

The Clementine spacecraft, launched in early 1994, recently completed a two-month lunar mapping mission in which it recorded high-resolution images over the entire surface of the moon. The attitude determination and control subsystems developed for the mapping phase of the mission are described. The vehicle's attitude determination subsystem consisted of a simple fixed-gain Kalman filter, uncoupled about each spacecraft axis, combining rate inputs from two solid-state optical gyros and attitude inputs from two wide field-of-view star trackers. The attitude control subsystem consisted of a simple proportional-integral-derivative algorithm operating on quaternion and rate feedback signals to provide pointing, tracking, and slewing functions. The primary actuating devices were three reaction wheels used for feedback error compensation and 12 thrusters used for occasional momentum dumping. During lunar mapping the attitude determination and control subsystems maintained vehicle pointing to within a three-axis rss value of 0.05 deg. On-orbit results are provided from outputs of the attitude determination filter, the lunar nadir-tracking controller, and the large-angle slew generator. Additionally, results are provided from a novel inertia estimator, which utilized sensor outputs during two slew maneuvers.

I. Introduction and Mission Overview

CLEMENTINE, the deep space program science experiment spacecraft developed by the Naval Research Laboratory (NRL) and cosponsored by the Ballistic Missile Defense Organization (BMDO) and NASA, was launched from Vandenberg Air Force Base on Jan. 25, 1994, using a Titan IIG launch vehicle. The Clementine spacecraft was designed, built, tested, and operated by NRL's Naval Center for Space Technology. Clementine's primary objective was to space-qualify lightweight imaging sensors and component technologies during its mission to lunar orbit and its flyby of the near-Earth asteroid Geographos. The Lawrence Livermore National Laboratory provided small, lightweight cameras and mission sensors to record high-resolution images in a wide spectrum of wavelengths. Included in the sensor package were two star tracker (ST) cameras, an ultraviolet/visible camera, a near-infrared camera, a long-wave infrared camera, a high-resolution camera, and a laser image detection and ranging camera. Specific characteristics of the sensor payload, as well as general descriptions and objectives of the Clementine mission, are provided in Refs. 1–3. A description of the mission astrodynamics is provided by Kaufman et al.[4]

Clementine was a three-axis stabilized spacecraft for the majority of its lifetime, with the exception being a brief spin-stabilized period in low Earth orbit (LEO) during ignition and burn of its solid rocket motor (SRM). During this spin period the vehicle was a prolate spinner, requiring active nutation control to suppress nutation angle growth and spin axis precession to control momentum vector walking. Reference 3 provides a complete description of the LEO phase of the mission. Under three-axis mode, the attitude determination and control system was required to perform attitude functions for lunar mapping, Earth and star pointing, momentum management, and attitude hold during orbit correction burns. Attitude determination was performed using two three-axis inertial measurement units (IMU) with periodic updates from the ST cameras. Attitude control was performed using proportional-integral-derivative (PID) control with reaction wheels and simple bang-bang control with jet thrusters. The thrusters were also utilized during momentum management and orbit correction burns.

In this paper we describe the attitude determination and control system (ADCS) for the Clementine spacecraft operating in lunar mapping mode and provide some on-orbit performance results during this phase of the mission. Descriptions of the vehicle configuration and the ADCS hardware package are provided in Sec. II. The Kalman filter-based attitude determination subsystem is described in Sec. III. A description of the three-axis control law design for pointing, tracking, and slewing the vehicle is described in Sec. IV. Included in that section is a simple strategy for estimating the vehicle moments of inertia on orbit. Some selected on-orbit results from the attitude determination filter, the control subsystem, and the inertia estimator are provided in Sec. V.

II. Spacecraft Configuration and ADCS Hardware

The Clementine spacecraft had two primary configurations during the course of its mission. The first configuration was maintained during a one-week checkout period while the vehicle was in LEO. In this initial state, Clementine's two solar panels were stored and the SRM was attached. Upon completion of checkout, the spacecraft was spin stabilized and the SRM was ignited to place the vehicle in a lunar trajectory. Immediately after the burn sequence, the SRM was jettisoned and the solar arrays were deployed and began coarse sun tracking. This final configuration, depicted in Fig. 1, was maintained for the remainder of the mission. The ADCS package for this final state consisted of 12 jet thrusters, 4 reaction wheels, 2 IMU, and 2 ST cameras. The vehicle mass and inertias for both configurations are provided in Table 1 (in the deployed state, the relative attitude of the solar panels was insignificant on the overall vehicle inertias).

To meet the goal of demonstrating emerging technologies using small, highly capable spacecraft, and to satisfy a demanding time constraint of two years from design to launch, the Clementine ADCS had to be designed in a simple, efficient manner to take advantage of new lightweight sensors and actuators, minimize required hardware and software, and keep costs low. Typically for this type of mission, narrow field-of-view ST cameras are used in conjunction

Received Dec. 12, 1994; revision received Dec. 12, 1995; accepted for publication Dec. 14, 1995.

*Senior Control Systems Engineer. Member AIAA.
†Subsystem Lead Engineer, Spacecraft Attitude Control Section. Member AIAA.
‡Aerospace Engineer, Spacecraft Attitude Control Section. Member AIAA.
§Section Head, Spacecraft Attitude Control Section. Member AIAA.

Table 1 Clementine mass and inertia properties

	Config. 1	Config. 2 (wet)	Config. 2 (dry)
Mass, kg	1647	456	233
Inertia, kg-m^2			
I_{xx}	199	93	66
I_{yy}	733	80	56
I_{zz}	736	107	77

Table 2 ADCS hardware mass

2 ST cameras	0.6 kg
2 IMU	1.2 kg
4 reaction wheels	11.1 kg
Total	12.9 kg

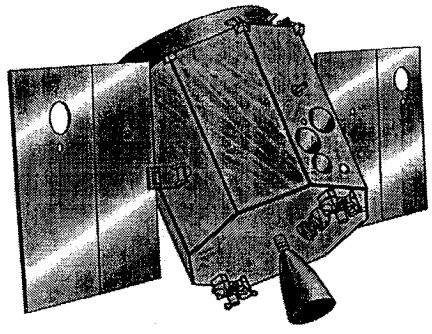

Fig. 1 Configuration of Clementine during lunar mapping.

with high-performance, low-drift gyros. For the Clementine mission, however, a system was selected to rely on two wide field-of-view, lightweight ST cameras, two relatively low-performance IMU for attitude propagation between ST updates, and four lightweight reaction wheels for primary actuation.

The ST cameras were part of the primary payload sensor package tested by this mission. These small, lightweight, wide field-of-view cameras provided full three-axis, lost-in-space attitude determination with a single image from either camera. The sensors transmitted an image to an image processor, which matched the brightest objects using an onboard star catalog. An attitude quaternion was then generated and sent to the attitude determination code. To ensure ST updates throughout the mission, the two cameras possessed no overlapping coverage (i.e., if one camera was pointing directly at the moon, the other camera would be directed into space). The ST cameras were aligned to the vehicle axes to within 0.01 deg prior to launch.

Two uniquely different small, lightweight IMUs were selected for the mission. These were the Litton LN200 IMU using interferometric fiber optic gyros and silicon accelerometers and the Honeywell lightweight advanced implementation technology IMU using ring laser gyros and Sundstrand RBA-500 accelerometers. The outputs of the gyros were delta angles and the outputs of the accelerometers were delta velocities. The gyros were capable of measuring up to 1000 deg/s with a nominal drift rate of 1 deg/h. The IMUs were aligned to the vehicle axes to within 0.01 deg prior to launch.

Four small Ball Aerospace reaction wheels with internal electronics were selected as the primary actuators while in three-axis control. Three of the wheels were orthogonally aligned to the vehicle axes, with a skewed fourth wheel acting as a backup. Hall-effect sensors were mounted to the wheel assemblies to provide wheel speed knowledge for momentum dumping; however, these sensors were not sufficient for use in a local feedback loop. The torque and momentum capabilities of the wheels were a modest 6 oz-in. and 2 N-m-s, respectively. The bearing friction ranged from 1 to 2 oz-in.

As seen in Table 2, the total mass of the primary ADCS hardware, comprising two ST cameras, two IMUs, and four reaction wheels was only 13 kg. In their as-built configuration, the Clementine mission was the first spaceflight test for all of the hardware just described.

III. Attitude Determination

Clementine's two IMUs provide redundant three-axis vehicle rotational delta angles at a frequency of 400 Hz. These signals were further processed to provide the ADCS system with an available three-axis signal at 20.83 Hz. It was assumed that the three delta angles are related to the IMU-measured vehicle body rates through the equation

$$\omega = \Delta/h - \boldsymbol{d}_{\text{est}} \tag{1}$$

where ω represents the body rate vector, Δ represents the delta-angle output vector from the IMU, $\boldsymbol{d}_{\text{est}}$ represents the vector of current estimates of the IMU rate biases (drift) along each axis, and h is the sample step size of 48 ms. In the following, we adopt the convention that the subscripts 1, 2, 3 of a vector's components correspond, respectively, to the x, y, z axes of the spacecraft. To obtain a measure of attitude the body rates are introduced into recursive quaternion propagation equations of the form

$$\boldsymbol{q}_k = [\mathbf{1}\cos(\lambda h/2) + \boldsymbol{\Gamma}\sin(\lambda h/2)/\lambda]\boldsymbol{q}_{k-1}$$

$$\boldsymbol{\Gamma} = \begin{bmatrix} 0 & \omega_3 & -\omega_2 & \omega_1 \\ -\omega_3 & 0 & \omega_1 & \omega_2 \\ \omega_2 & -\omega_1 & 0 & \omega_3 \\ -\omega_1 & -\omega_2 & -\omega_3 & 0 \end{bmatrix} \tag{2}$$

$$\lambda = \sqrt{\omega_1^2 + \omega_2^2 + \omega_3^2}$$

where $\boldsymbol{q}_k$ represents the quaternion estimate at time t_k and $\mathbf{1}$ is the 4×4 identity matrix. Of course, over a period of time this estimated attitude will drift off from the true attitude because of errors in the estimated IMU rate biases as well as IMU angular random walk (noise). The ST is used to compensate for the IMU biases and, in effect, reset the estimated quaternions periodically. This is accomplished by combining both the IMU-based attitude quaternion and ST-based attitude quaternion into a simple fixed-gain Kalman filter as described next.

The primary goal of the IMU/ST filter design is to combine the two sensor outputs in such a manner as to provide an updated attitude estimate from each star sensor measurement (which is nominally sampled every 10 s) as well as an estimate of the IMU rate biases along each axis. These biases are then canceled from the IMU signals [see Eq. (1)] to improve the quality of the recursive quaternion equations between each ST measurement. We chose to design the filter based on the error quaternion obtained from

$$\boldsymbol{Q} = \boldsymbol{q} \otimes \boldsymbol{q}_e \tag{3}$$

where $\otimes$ is the quaternion multiplier, $\boldsymbol{Q}$ represents the desired attitude quaternion, and $\boldsymbol{q}_e$ represents the error quaternion. Upon utilizing the quaternion algebraic identities

$$(\boldsymbol{a} \otimes \boldsymbol{b}) \otimes \boldsymbol{c} = \boldsymbol{a} \otimes (\boldsymbol{b} \otimes \boldsymbol{c}) \tag{4a}$$

$$\boldsymbol{a} \otimes \boldsymbol{b} = \boldsymbol{b} \otimes \boldsymbol{a} + 2(\boldsymbol{a} \times \boldsymbol{b}, 0) \tag{4b}$$

where $\times$ represents the vector cross-product operator, results similar to those given by Lefferts et al.[5] are obtained by differentiating Eq. (3) with respect to time, yielding

$$\dot{\boldsymbol{q}}_e = \tfrac{1}{2}\boldsymbol{q}_e \otimes (\boldsymbol{W} - \omega_{\text{true}}, 0) - (\omega_{\text{true}} \times \boldsymbol{q}_e, 0) \tag{5}$$

where $\boldsymbol{W}$ represents the commanded rate vector and ω_{true} represents the actual vehicle rate vector. The primary difference between this formulation and the error formulation developed in Ref. 5 is that we have chosen to use the error signal between the command and the current estimated attitude as opposed to the error signal between the ST attitude and the current estimated attitude. If we make the assumption that the body rates and the error quaternion are small, we obtain approximate uncoupled kinematics in the form

$$\dot{\boldsymbol{q}}_e \approx \tfrac{1}{2}(\boldsymbol{W} - \omega_{\text{true}}) \tag{6a}$$

$$\dot{q}_{e4} \approx 0 \tag{6b}$$

Choosing a model of the IMU in the form

$$\omega_{\text{true}} = \Delta/h - \boldsymbol{d} - \text{IMU noise} \tag{7}$$

allows us to define governing kinematic relationships such that

$$\dot{\boldsymbol{q}}_e = \tfrac{1}{2}(\boldsymbol{W} - \Delta/h) + \tfrac{1}{2}\boldsymbol{d} + \tfrac{1}{2}(\text{IMU noise}) \tag{8a}$$

$$\dot{\boldsymbol{d}} = \text{drift process noise} \tag{8b}$$

where the drift process noise is assumed to be a zero-mean, white noise sequence. These kinematic equations represent approximate propagation equations of the error quaternion estimate between discrete ST sample times. At each ST measurement, these equations are appended with update equations of the form

$$\boldsymbol{q}_e^+ = \boldsymbol{q}_e^- + K_q({}_{\text{ST}}\boldsymbol{q}_e - \boldsymbol{q}_e^-) \tag{9a}$$

$$q_{e4} = \sqrt{1 - q_{e1}^2 - q_{e2}^2 - q_{e3}^2} \tag{9b}$$

$$\boldsymbol{d}^+ = \boldsymbol{d}^- + K_d({}_{\text{ST}}\boldsymbol{q}_e - \boldsymbol{q}_e^-) \tag{9c}$$

where ${}_{\text{ST}}\boldsymbol{q}_e$ represents the error quaternion between the commanded quaternion and the ST output (which is a three-axis attitude quaternion measurement), and K_q and K_d are scalar filter gains. Equations (8) and (9) represent three sets of uncoupled Kalman filter equations with states $\{q_{e1}, d_1\}$, $\{q_{e2}, d_2\}$, and $\{q_{e3}, d_3\}$.

Some discussion of the unique characteristics of this filter is warranted. First, it is clear that the 2×2 state matrix and the 1×2 measurement matrix associated with these equations are both simple, constant coefficient matrices, yielding a steady-state solution for the two gains and, as a consequence, a very simple computational algorithm for the filter. These gains become a function of the IMU and ST noise levels, which are set by hardware, and the drift process noise levels, which are chosen by the designer to obtain desirable drift estimate time histories. It is also clear from Eq. (9) that if both gains are set to zero the attitude estimate is based solely on IMU information and the drift estimate remains constant. Furthermore, if K_q is set to unity, then the IMU-based quaternion estimate is simply replaced by the ST-based estimate at each star sensor sample time and no filtering of the ST signal takes place. Additionally, the approximate propagation equations given in Eq. (8) are utilized only for determining the steady-state filter gains; actual on-orbit propagation is more accurately achieved from use of Eqs. (2) and (3), which are being recursively solved for attitude and error quaternions at each IMU sample time without the assumptions that body rates and errors are small. The quaternion estimates that are used to update Eq. (2) after each ST measurement can be obtained directly from Eq. (3), given $\boldsymbol{Q}$ and $\boldsymbol{q}_e$ from the filter. Finally, if a vector to a star is measured (as is usually the case with standard narrow field-of-view cameras) instead of the three-axis attitude measurements from the wide field-of-view Clementine cameras, and if the assumption of small body rates is dropped, the resulting filter requires calculation of six time-varying gains,[5] as opposed to the two fixed gains used here.

The applicability of the uncoupled, steady-state Kalman filter just described lies in the assumptions that the attitude errors and body rates are small. These assumptions are certainly valid in an inertial pointing mode or a lunar mapping mode, in which the commanded vehicle rates are low and well within typical controller bandwidths. During a relatively fast attitude reorientation maneuver, however, the associated rates and tracking errors will likely be too large for these assumptions to be valid. During these maneuvers the filter can either be placed in an inactive state by setting K_q to unity and K_d to zero, or can simply operate in an invalid mode for the duration of the slew. For the Clementine mission we chose to operate the filter continuously, allowing for filter error transients to subside upon completion of slew maneuvers.

IV. Attitude Control During Moon Mapping

A typical moon mapping sequence for Clementine consisted of the following stages: 1) a large-angle slew maneuver to nadir-pointing attitude, 2) 1.5 h of nadir tracking while mapping the lunar surface, 3) a large-angle slew to Earth-pointing attitude, and 4) 3.5 h of Earth pointing while transmitting data. During these stages the spacecraft utilized the reaction wheels to provide three-axis control. Design of the reaction wheel control system was based on both nonlinear Lyapunov stability theory and classical linear principles. The nonlinear analysis resulted in a globally stable form of the feedback control system under the assumptions that sensor and actuator dynamics and system delays are negligible and body rates are small. The linear analysis provided numerical values for the feedback gains to ensure desired stability margins and disturbance rejection using single-loop approximations.

Quaternion Feedback Control

The governing nonlinear equations for the spacecraft and reaction wheels can be written as

$$\dot{\boldsymbol{\omega}} = -(\boldsymbol{I} - \boldsymbol{I}_w)^{-1}\left(\boldsymbol{B}^{-1}\boldsymbol{u}_w + \tilde{\boldsymbol{\omega}}\boldsymbol{H} - \boldsymbol{u}_{\text{ext}}\right) \tag{10a}$$

$$\boldsymbol{H} = \boldsymbol{I}\boldsymbol{\omega} + \boldsymbol{B}^{-1}\boldsymbol{I}_w\boldsymbol{\Omega} \tag{10b}$$

$$\dot{\boldsymbol{\Omega}} = \boldsymbol{I}_w^{-1}\boldsymbol{u}_w - \boldsymbol{B}\dot{\boldsymbol{\omega}} \tag{10c}$$

where $\boldsymbol{\Omega}$ is the wheel speed vector in the wheel frame, $\boldsymbol{u}_w$ is the torque vector applied to the wheels in the wheel frame, $\boldsymbol{u}_{\text{ext}}$ is the external torque vector, $\boldsymbol{I}$ is the vehicle inertia matrix with fixed wheels, $\boldsymbol{I}_w$ is the diagonal wheel axial inertia matrix, $\tilde{\boldsymbol{\omega}}$ is the skew symmetric body rate matrix, $\boldsymbol{B}$ is the transformation matrix from the body frame to the wheel frame, and $\boldsymbol{H}$ is the system momentum vector. Following the analyses of Vadali and Junkins[6] and Wie and Barba,[7] Lyapunov stability theory can be used to show that the quaternion feedback control law given in the form

$$\boldsymbol{B}^{-1}\boldsymbol{u}_w = -\tilde{\boldsymbol{W}}\boldsymbol{H} - (\boldsymbol{I} - \boldsymbol{I}_w)\dot{\boldsymbol{W}} - g_D(\boldsymbol{W} - \boldsymbol{\omega}) - g_P\boldsymbol{q}_e \tag{11}$$

will provide asymptotic stability with respect to a tracking signal (defined by the commanded rate vector $\boldsymbol{W}$) for the system described in Eq. (10) in the absence of modeling errors, sensor and actuator dynamics, and system delays. The constant feedback gains g_D and g_P are chosen to be equal about each axis because the inertia distribution is not widely separated during the lunar mapping phase of the mission. If the commanded rates are small and the system momentum is maintained at a low level (through periodic momentum dumping), the first term in the preceding equation can be treated simply as a disturbance and omitted from the feedback law. The second term, which represents acceleration feedforward, can also be omitted as long as the bandwidth of the feedback system (dictated by the choice of g_P and g_D) is sufficient to limit tracking errors to within a desired level. Although the resulting feedback system will no longer be stable with respect to a general tracking signal because of the low system type, it will remain stable with respect to a fixed attitude command (of course, even the feedforward system will not be stable with respect to a tracking signal in practice, because of errors in the inertia matrix). Additionally, to reject constant (or nearly constant) disturbances such as wheel friction we included a small integral feedback term in Eq. (11), resulting in the final PID control law

$$\boldsymbol{B}^{-1}\boldsymbol{u}_w = -g_D(\boldsymbol{W} - \boldsymbol{\omega}) - g_P\boldsymbol{q}_e - g_I\int \boldsymbol{q}_e\,\mathrm{d}t \tag{12}$$

Numerical values for the three feedback gains are chosen based upon classical linear theory as described next.

Feedback Gain Design

To design the three PID feedback gains, we chose to examine a single axis of the system and use an average value of the inertia distribution as the loop inertia. The gains are then designed to satisfy open-loop phase margin at a prescribed crossover frequency (ω_c) and disturbance rejection at a prescribed rejection frequency ($\omega_r \ll \omega_c$). Since the simplified plant transfer function is $1/Is^2$ (with -180 deg of phase), the controller must provide additional phase equal to the desired phase margin (φ_m) and gain equal to $I\omega_c^2$ (1/plant gain)

at the crossover frequency. For a given value of g_I, it can be shown that the other gains must satisfy the relations

$$g_P = I\omega_c^2 \cos(\varphi_m) \tag{13a}$$

$$g_D = g_I/\omega_c^2 + I\omega_c \sin(\varphi_m) \tag{13b}$$

The value of g_I can be chosen to provide a prescribed level of disturbance rejection (μ_d) at the rejection frequency ω_r using the relation

$$g_I = \omega_r/\mu_d \tag{13c}$$

where it is assumed that ω_r is much smaller than ω_c. Choosing the phase margin to be 40 deg at a crossover frequency of 0.05 Hz and the disturbance rejection level to be 40 dB at a rejection frequency of 80 μHz results in gains of 6.53, 17.67, and 0.05 for g_P, g_D, and g_I, respectively. Standard single-axis Bode and disturbance rejection plots for this system (with inclusion of high bandwidth sensors and actuators and zero-order-hold delays) demonstrate that the desired crossover frequency, stability margin, and disturbance rejection level are satisfied with this set of gains.

Large-Angle Slew Command Generator

Large-angle rest-to-rest slew maneuvers were performed through single-axis rotation of the spacecraft about a skewed Euler axis. The onboard computer first calculates the Euler angle ϕ_f and Euler axis of rotation $\boldsymbol{e}$ that will take the vehicle from its current quaternion to the desired quaternion. A commanded bang-coast-bang time history of the slew is then determined such that the wheel speeds and the applied torques are within prescribed bounds.

If it is assumed that the vehicle nonlinear dynamics are negligible, then we obtain approximate equations for the torque vector

$$\boldsymbol{u}_w \approx -\boldsymbol{B}(\boldsymbol{I} - \boldsymbol{I}_w)\dot{\boldsymbol{\omega}} \approx -\boldsymbol{B}(\boldsymbol{I} - \boldsymbol{I}_w)\boldsymbol{e}\ddot{\phi} \tag{14}$$

where it has also been assumed that the vehicle rate vector follows (is parallel to) the Euler axis. Within the framework of these assumptions, the value of an acceleration parameter α can be chosen as

$$\alpha = \ddot{\phi}_{\max} = u_{\max}/\max[\boldsymbol{B}(\boldsymbol{I} - \boldsymbol{I}_w)\boldsymbol{e}] \tag{15}$$

where $u_{\max}$ is a user-defined maximum allowable wheel torque level. The commanded angular acceleration and phase-plane path about the Euler axis is chosen as shown in Fig. 2, where the on time (t_{on}) and slew time (t_s) are defined subsequently. The commanded rate and attitude profiles then become

$$\boldsymbol{W}(t) = \boldsymbol{e}\dot{\phi} \tag{16a}$$

$$\boldsymbol{Q}(t) = [\boldsymbol{e}\sin(\phi/2), \cos(\phi/2)] \tag{16b}$$

where $\boldsymbol{Q}$ represents the commanded quaternion history relative to the initial quaternion. These commands are introduced into the feedback control law of Eq. (12) to obtain the wheel torques.

The on time and slew time depicted in Fig. 2 are determined such that the reaction wheel speeds remain bounded. For a vehicle initially at rest with no external disturbances, the wheel speed time histories during the course of a slew can be determined from conservation of angular momentum, yielding

$$\boldsymbol{\Omega}(t) = \boldsymbol{BC}(\boldsymbol{Q})\boldsymbol{B}^{-1}\boldsymbol{\Omega}_0 - \boldsymbol{I}_w^{-1}\boldsymbol{BIe}\dot{\phi} \tag{17}$$

where $\boldsymbol{\Omega}_0$ is the initial wheel speed vector and $\boldsymbol{C}(\boldsymbol{Q})$ is the direction cosine matrix relating the current attitude to the initial attitude. An iterative time-domain solution to Eq. (17) can be performed until a valid slew time and on time are calculated such that the wheel speeds remain below a specified maximum value. The two critical times are related through the expression

$$t_{on} = \tfrac{1}{2}\left[t_s - \sqrt{t_s^2 - 4\phi_f/\alpha}\right] \tag{18}$$

A good starting point for the iterative solution is to assume the coast time to be zero (pure bang-bang control), resulting in a slew time of $2\sqrt{(\phi_f/\alpha)}$. The slew time can then be increased incrementally until the wheel speed bounds are satisfied. This iterative approach for calculating the slew profile is depicted in the flow chart of Fig. 3.

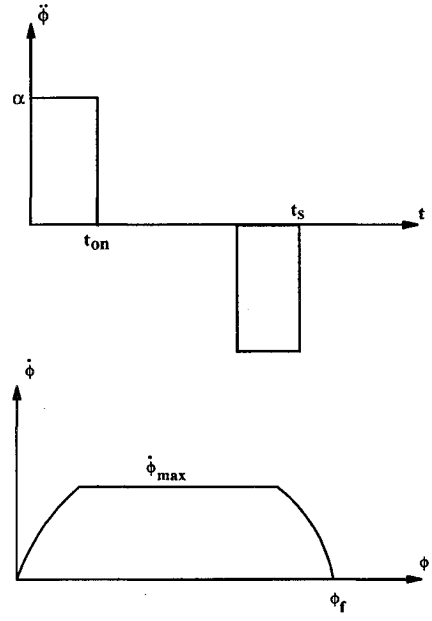

Fig. 2 Commanded Euler angle history for large-angle slews.

Combining the reaction wheel control system described with the attitude determination filter from Sec. IV yields the ADCS block diagram provided in Fig. 4. The solid lines in the figure represent measurable or calculated signals and the broken lines represent unknown signals. The IMU and ST measurement errors include noise, biases, misalignments, and scale factor inaccuracies. The software toggle switch at the left end of the diagram remains in the upper position between ST updates and drops to the lower position every 10 s to incorporate the filtered IMU/ST attitude estimate.

Thruster Control

During the lunar mapping phase of the Clementine mission, the hydrazine thrusters were utilized for two functions. They provided coarse attitude control during orbit correction burns and momentum management to release momentum from the wheels. A 110-lbf bipropellant motor was used for orbit correction burns, with typical burns lasting anywhere from a few seconds to a few minutes. During the burn sequence a simple on–off control logic operating on a combined attitude and rate error signal was implemented for the thrusters. An attitude deadband of approximately 0.25 deg was maintained. Momentum management was active at all times during operation of the reaction wheels. The system was designed to autonomously monitor wheel speeds, determine if momentum dumping was required, and execute thruster pulses. Pulses were fired to reduce the entire system momentum, not just that of a single wheel.

On-Orbit Spacecraft Inertia Estimation

The moments of inertia of a spacecraft change throughout its mission because of component jettisoning, appendage reorientation, and fuel expulsion. During the lunar mapping phase of its mission, Clementine's inertias decreased by approximately 10–20% mainly because of fuel expulsion. The feedback system possessed sufficient stability margin to accept these changes, and so gain scheduling was not required and the exact inertia values were not needed. For spacecraft, however, which implement model-based feedforward controllers and experience significant inertia changes, it may be of interest to utilize an on-orbit strategy to estimate these parameters. Following the approach by Creamer,[8] we describe one such strategy that utilizes reaction wheel speeds and vehicle rates as inputs to the estimator.

For a momentum-exchange control system such as that used on Clementine, large-angle slew maneuvers are directly affected by

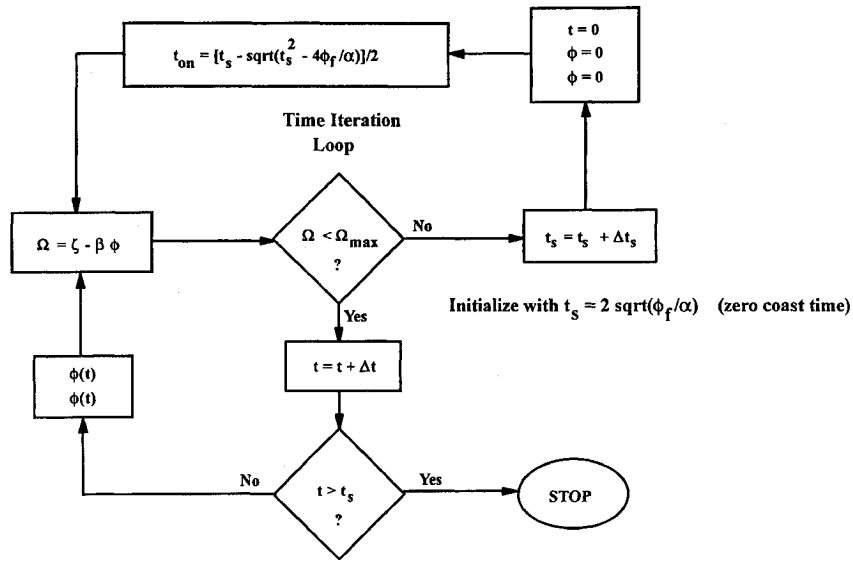

Fig. 3 Large-angle slew flow chart.

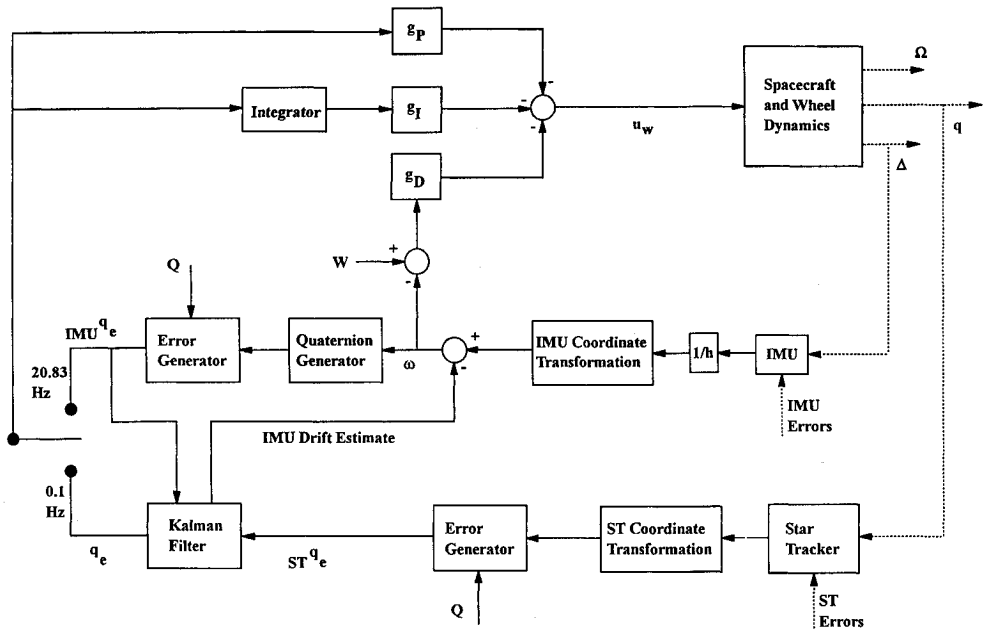

Fig. 4 Clementine ADCS block diagram for lunar mapping.

the vehicle's inertias through wheel speeds and body rates. Using this information, estimates of the inertias can be accomplished from a single maneuver via conservation of angular momentum. From Eq. (10b), the angular momentum of the vehicle in body coordinates is given as

$$\boldsymbol{H}_b = \boldsymbol{I}\boldsymbol{\omega} + \boldsymbol{B}^{-1}\boldsymbol{I}_w\boldsymbol{\Omega} = \boldsymbol{C}(\boldsymbol{q})\boldsymbol{H}_I \tag{19}$$

where $\boldsymbol{H}_b$ is the momentum vector in body coordinates, $\boldsymbol{H}_I$ is the constant momentum vector in inertial coordinates (assuming no external torques), and $\boldsymbol{C}(\boldsymbol{q})$ is the transformation matrix from the inertial frame to the body frame (with the quaternions determined from integration of the body rates). Equation (19) is linear in the unknown parameters of the inertia matrix and the constant momentum vector. By rearranging and introducing sensor measurements we obtain the equation

$$\boldsymbol{B}^{-1}\boldsymbol{I}_w\boldsymbol{\Omega}_w = \boldsymbol{C}(\boldsymbol{q})\boldsymbol{H}_I - \boldsymbol{I}\boldsymbol{\omega}_{\text{gyro}} + \boldsymbol{n} \tag{20}$$

where $\boldsymbol{\Omega}_w$ represents wheel speed measurements, $\boldsymbol{\omega}_{\text{gyro}}$ represents body rate measurements, and $\boldsymbol{n}$ is a noise vector with statistics obtained from both the wheel speed noise and the gyro noise. We have neglected second-order effects such as scale factor, misalignment, and bias errors in the measurements. If we assume that the products of inertia are much smaller than the moments of inertia we can define a six-state parameter vector $\boldsymbol{x}$ such that

$$\boldsymbol{x}^T = \{H_x \quad H_y \quad H_z \quad I_{xx} \quad I_{yy} \quad I_{zz}\} \tag{21}$$

which can be determined from a recursive linear estimator of the form

$$\boldsymbol{x}_k = \boldsymbol{x}_{k-1} + \boldsymbol{K}_k(\boldsymbol{y}_k - \boldsymbol{A}_k\boldsymbol{x}_{k-1}) \tag{22a}$$

$$\boldsymbol{K}_k = \boldsymbol{P}_{k-1}\boldsymbol{A}_k^T\left(\boldsymbol{A}_k\boldsymbol{P}_{k-1}\boldsymbol{A}_k^T + \boldsymbol{R}_k\right)^{-1} \tag{22b}$$

$$\boldsymbol{P}_k = (\boldsymbol{1} - \boldsymbol{K}_k\boldsymbol{A}_k)\boldsymbol{P}_{k-1} \tag{22c}$$

where $\boldsymbol{K}$ represents the Kalman gain matrix, $\boldsymbol{P}$ represents the parameter error covariance matrix, $\boldsymbol{1}$ is the identity matrix, $\boldsymbol{y}$ is the

left-hand side of Eq. (20), $\boldsymbol{R}$ is the measurement error covariance matrix, and $\boldsymbol{A}$ is the parameter sensitivity matrix defined as

$$A = \begin{bmatrix} C_{11} & C_{12} & C_{13} & -\omega_{x\_gyro} & 0 & 0 \\ C_{21} & C_{22} & C_{23} & 0 & -\omega_{y\_gyro} & 0 \\ C_{31} & C_{32} & C_{33} & 0 & 0 & -\omega_{z\_gyro} \end{bmatrix} \quad (23)$$

Solving Eq. (22) during a large-angle slew maneuver (or as a post-processor) results in a recursive estimate of the three moments of inertia as long as the slew Euler axis has components along each of the vehicle axes (the parameters must be observable). On-orbit results using the Clementine spacecraft as a testbed are presented in the following section.

V. On-Orbit Performance

In this section we provide some selected on-orbit results obtained from the Clementine spacecraft during its lunar mapping mission. Specifically, we will demonstrate the performance of the attitude determination Kalman filter, the quaternion feedback tracking algorithm, the large-angle slew command generator, and the vehicle inertia estimator.

As described in Sec. IV, the Kalman filter design resulted in a simple two-state attitude determination filter for each body axis, with the states representing small error quaternions and IMU rate biases. Of particular interest here are the estimates of the IMU biases, which are canceled from the rate outputs prior to integrating the quaternion kinematic equations. Provided in Fig. 5 are typical drift estimates from one of the gyro units. We first initialized the estimates to zero and then activated the filter to demonstrate convergence. Upon convergence of the filter, any further changes in the drift estimates were primarily because of temperature gradients while the IMU crossed in and out of sunlight. The z component of drift was well outside its nominal specification of 1 deg/h. This large value would have significantly degraded pointing and tracking performance in the absence of the Kalman filter.

The pointing and tracking requirements for the Clementine spacecraft, established by the science payload team, were to maintain attitude control errors under a root-sum-square value of 0.05 deg. During lunar mapping, quaternion and rate commands were generated on orbit to orient the vehicle sensor axis in the direction of nadir. As observed from the typical lunar mapping sequence in Fig. 6, the 3-sigma pointing errors were within the specifications for a large majority of the sequence. The specific orbit depicted in Fig. 6 consisted of an 80-min nadir-tracking mapping sequence with the remainder of the orbit used for Earth communication and star pointing. During a typical mapping sequence, the vehicle underwent rotations of approximately 180 deg (tracking nadir) and the skewed wheels exhibited zero-speed crossings. It is clear from Fig. 6 that the friction disturbances in the wheels were effectively canceled with the integral feedback terms of the control law (otherwise, there would exist significant pointing error biases).

The large-angle slew command generator was activated during vehicle reorientations such as moon-to-Earth, Earth-to-moon, and star pointing maneuvers. As described in Sec. IV, these commands were designed to satisfy wheel speed and torque saturation constraints. A typical large-angle maneuver is provided in Figs. 7 and 8 in terms of the attitude quaternions and the wheel speed histories. This maneuver consisted of a 160-deg slew about an Euler axis defined in body coordinates as (0.68321, 0.19091, −0.70482), with an on time of 37 s and a slew time of 269 s. It is clear that the on-orbit performance was in excellent agreement with theory, and the wheel speed constraint, which was set at 1200 rpm for this particular maneuver, was satisfied.

The inertia estimation algorithm described in Sec. IV was applied to Clementine to test its potential for use in future adaptive spacecraft control systems. Two slew maneuvers, defined in Table 3, were used for this study. Since the unknown parameters (momentum and inertias) appear linearly in the estimator, their initial estimates are not critical. We arbitrarily chose to set each inertia value to 100 kg-m^2 and the momentum vector to null. Results given in Fig. 9 show that the final inertia estimates from each slew agree to within 3% or less. Small differences in these final values are attributed to nonzero products of inertia, which were assumed to be negligible. These results closely agreed with ground-based measured and calculated values of moments of inertia, demonstrating the potential for such a simple estimation algorithm in future missions.

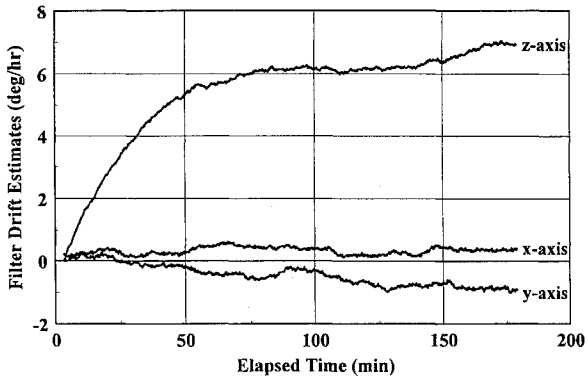

Fig. 5 Typical on-orbit gyro drift estimates.

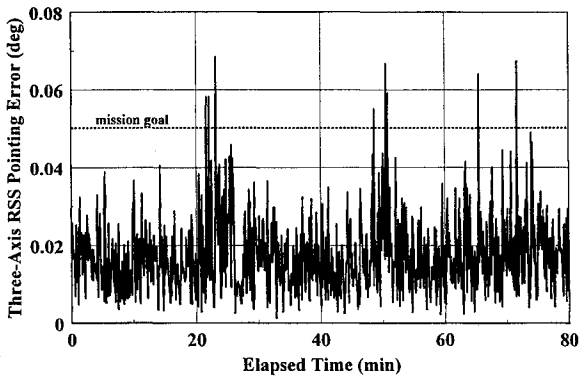

Fig. 6 Typical on-orbit pointing errors during lunar mapping.

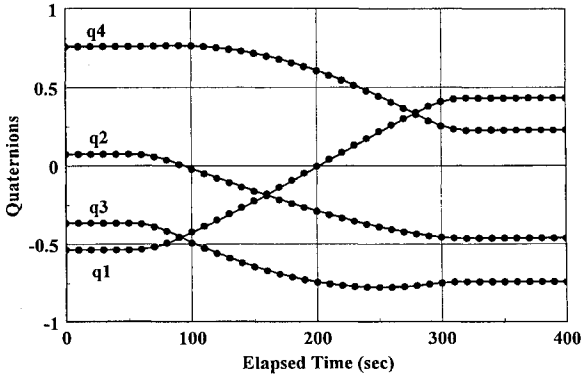

Fig. 7 On-orbit quaternions during typical large-angle slew; ——, theory and •, on orbit.

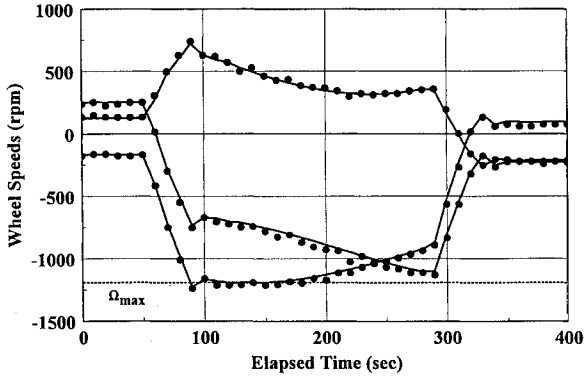

Fig. 8 On-orbit wheel speeds during typical large-angle slew; ——, theory and •, on orbit.

Table 3 Slew maneuvers for inertia estimation

	Slew 1	Slew 2
Euler axis	(−0.58656, −0.28106, 0.75958)	(−0.68334, 0.19096, −0.70468)
Euler angle, deg	148.64	159.74

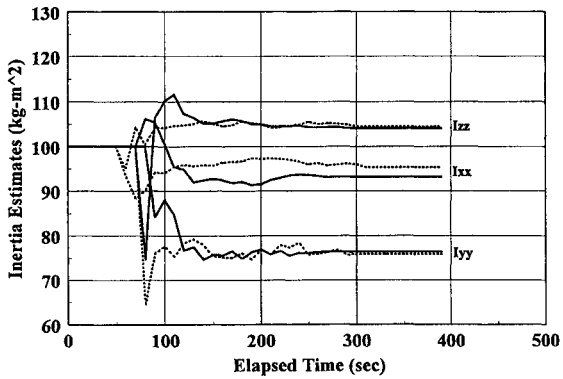

Fig. 9 Estimation of Clementine inertias using on-orbit slew data; ——, slew 1 and •, slew 2.

VI. Conclusions

The Clementine spacecraft, cosponsored by BMDO and NASA, recently completed a successful two-month lunar mission in which it mapped the entire surface of the moon in unprecedented detail using advanced, lightweight sensors. During this phase the vehicle was three-axis stabilized using lightweight reaction wheels and combined IMU/ST measurements for attitude determination and control. We described the fixed-gain Kalman filter used for attitude determination and the quaternion feedback control law used for pointing, tracking, and slewing. The two-state, uncoupled Kalman filter (applied about each vehicle axis) represented a simplified version of a general six-state coupled filter. The quaternion feedback gains were selected using a classical PID controller to ensure sufficient stability margin and disturbance rejection. The large-angle slew command generator was designed to satisfy wheel torque and momentum constraints using a bang-coast-bang profile. We also described a novel spacecraft inertia estimator, which utilizes wheel speed and body rate measurements to estimate inertias and system momentum using a single slew maneuver. On-orbit results were included to demonstrate the performance of the filter, controller, and inertia estimator.

Acknowledgments

The authors wish to thank Robert Stapleford of Space Applications Corporation in El Segundo, CA, for his many helpful and enlightening suggestions during the course of the ADCS design stage and Samuel Hollander of the NRL for his review of the manuscript.

References

[1]Rustan, P. L., "Clementine: Mining New Uses for SDI Technology," *Aerospace America*, Vol. 1, Jan. 1994, pp. 38–41.

[2]Regeon, P. A., Chapman, R. J., and Baugh, R., "Clementine—The Deep Space Program Science Experiment (DSPSE)," IAA International Conf. on Low-Cost Planetary Missions, Johns Hopkins Univ. Applied Physics Lab., Laurel, MD, April 1994.

[3]DeLaHunt, P., Gates, S., Levenson, M., and Creamer, G., "The Clementine Attitude and Control System," AIAA/USU 8th Annual Conf. on Small Satellites, Logan, UT, Aug.–Sept. 1994.

[4]Kaufman, B., Middour, J., Dasenbrock, R., and Campion, R., "The Deep Space Program Science Experiment Mission: Astrodynamics Mission Planning," 44th Congress of the International Astronautical Federation, Graz, Austria, Oct. 1993.

[5]Lefferts, E. J., Markley, F. L., and Shuster, M. D., "Kalman Filtering for Spacecraft Attitude Estimation," *Journal of Guidance, Control, and Dynamics*, Vol. 5, No. 5, 1982, pp. 417–429.

[6]Vadali, S. R., and Junkins, J. L., "Optimal Open-Loop and Stable Feedback Control of Rigid Spacecraft Attitude Maneuvers," *Journal of the Astronautical Sciences*, Vol. 32, No. 2, 1984, pp. 105–122.

[7]Wie, B., and Barba, P. M., "Quaternion Feedback for Spacecraft Large Angle Maneuvers," *Journal of Guidance, Control, and Dynamics*, Vol. 8, No. 3, 1985, pp. 360–365.

[8]Creamer, N. G., "Applications of Self-Tuning Control for Spacecraft Tracking: Theory and Experiment," 1994 American Control Conf., Baltimore, MD, June–July 1994.